

# Mass spectrum of $1^{-+}$ exotic mesons from lattice QCD

M. S. Cook\* and H. R. Fiebig†  
*Department of Physics, Florida International University,  
Miami, Florida, USA 33199*  
(Dated: February 8, 2020)

Time correlation functions of a hybrid exotic meson operator, with  $J^{PC} = 1^{-+}$ , generated in quenched lattice QCD are subjected to a (Bayesian) maximum entropy analysis. Five distinct spectral levels are uncovered. Their extrapolation into the physical pion mass region suggests a possible relationship to experimentally known states  $\pi_1(1400)$  and  $\pi_1(1600)$ , and also to a state in the 2 GeV region carrying the same quantum numbers.

PACS numbers: 12.38.Gc, 13.25.-k

## I. INTRODUCTION

Quantum chromodynamics (QCD) in principle permits the existence of hadrons containing both quarks and valence gluons. These are commonly known as hybrids. For example, in the meson sector, the presence of explicit glue allows for states with quantum numbers  $J^{PC} = 1^{-+}$ . The standard quark model cannot describe a meson with the above quantum numbers. Hadrons with this feature are called exotic. Other exotic states are possible [1], however, in this article we will solely consider the  $1^{-+}$  hybrid exotic meson.

According to [2] experimentally established  $1^{-+}$  mesons are  $\pi(1400)$  and  $\pi(1600)$ . Several experimental programs currently focus on studies of exotic hadrons in general.

On the theoretical side we expect the lattice formulation of QCD, being a first-principles approach, to eventually yield the properties of hybrid exotics such as masses and decay widths. Studies in this area have been but a few [3, 4, 5, 6, 7, 8, 9, 10]. Results hint at masses in the 1.4 GeV region [4], and also at a state close to 1.9 GeV [5, 7].

In the present article we examine the mass spectrum of  $1^{-+}$  mesons based on lattice QCD. We utilize the outcome of a numerical simulation, gauge field configurations and quark propagators, which had been previously generated to study hybrid exotic decay widths [7].

The novel feature here is the use of Bayesian analysis, more precisely the maximum entropy method (MEM) [11]. This analysis tool enables us to utilize the entire range of lattice time slices, thus eliminating the necessity for a subjective choice of a time interval defining a plateau in the effective mass function, an approach almost universally used as an analysis method to ex-

tract hadron masses. When all time slices are utilized, on a given lattice volume, the method delivers unambiguous results, free from subjective choices of effective mass plateaus. In addition, the MEM is quite naturally adapted to multiple states, if present. We will particularly rely on this feature to uncover the  $1^{-+}$  hybrid exotic meson mass spectrum, up to somewhat above 2 GeV.

## II. LATTICE SIMULATION

In the context of the decay width calculation [7] it was argued that systematic errors would likely dominate the final result. For this reason the lattice action and lattice sizes were selected to keep the numerical effort moderate. Although such a constraint would not seem to be necessary for our present aim of ‘just’ extracting spectral masses, we find that the lattices and quark propagators generated in [7] give surprisingly relevant results.

Thus, we here present the  $1^{-+}$  exotic hybrid mass spectrum based on the Wilson gauge field action used with Wilson fermions, in the quenched approximation, on an anisotropic lattice of size  $12^3 \times 24$ . The bare aspect ratio is  $a_s/a_t = 2$ , with  $a_s$  being the spatial and  $a_t$  the temporal lattice constants. Simulations were done at one value of a global gauge coupling  $\beta = 6.15$  and four values of global hopping parameters  $\kappa$ , as they appear in Tab. I below. We refer the reader to [7] for a precise definition of these global parameters.

In order to set the physical mass scale, standard local zero-momentum meson operators of the form

$$O_X(t) = \sum_{\vec{x}} \bar{d}_a(\vec{x}t) \Gamma u_a(\vec{x}t), \quad (1)$$

where  $a$  is color, were employed for the pseudoscalar meson  $X = \pi, \Gamma = \gamma_5$ , the vector meson  $X = \rho, \Gamma = \gamma_i$ , and the  $a_1$  meson  $X = a_1, \Gamma = \gamma_i \gamma_5$ . where  $i = 1, 2, 3$  are spatial directions.

For an operator coupling to  $1^{-+}$  hybrid meson states, which we collectively refer to with  $h$ , we follow [5] and

\*mcook003@fiu.edu

†fiebig@fiu.edu; This material is based on work supported by the U.S. National Science Foundation under Grant No. PHY-0300065 and upon resources provided by the Lattice Hadron Physics Collaboration through the SciDac program of the U. S. Department of Energy.

use

$$O_h(t) = \sum_{1 \leq i < j \leq 3} \sum_{\vec{x}} \bar{d}_a(\vec{x}t) \gamma_i u_b(\vec{x}t) [F_{ij}^{ab}(\vec{x}t) - F_{ij}^{\dagger ab}(\vec{x}t)]. \quad (2)$$

Here  $a, b$  denote color indices and  $F_{ij}(x)$  is a product of  $SU(3)$  link matrices arranged in a clover pattern

$$\begin{aligned} F_{\mu\nu}(x) &= U_\mu(x)U_\nu(x + \hat{\mu})U_\mu^\dagger(x + \hat{\nu})U_\nu^\dagger(x) \\ &+ U_\nu(x)U_\mu^\dagger(x - \hat{\mu} + \hat{\nu})U_\nu^\dagger(x - \hat{\mu})U_\mu(x - \hat{\mu}) \\ &+ U_\mu^\dagger(x - \hat{\mu})U_\nu^\dagger(x - \hat{\mu} - \hat{\nu})U_\mu(x - \hat{\mu} - \hat{\nu})U_\nu(x - \hat{\nu}) \\ &+ U_\nu^\dagger(x - \hat{\nu})U_\mu(x - \hat{\nu})U_\nu(x + \hat{\mu} - \hat{\nu})U_\mu^\dagger(x), \end{aligned} \quad (3)$$

which is used in the spatial planes only thus employing magnetic type gluons, in the rest frame.

The parity transformation  $\mathcal{P}$  applied to (2) gives  $\mathcal{P}O_h(t)\mathcal{P}^{-1} = -O_h(t)$ , as it should. This relation relies on  $\mathcal{P}U_i(\vec{x}, t)\mathcal{P}^{-1} = U_{-i}(-\vec{x}, t)$  for  $i = 1, 2, 3$ , using the notation of Ref. [12]. At the quantum level the corresponding propagator respects exact (negative) parity because the (quenched) gauge field action  $S[U]$  is translationally invariant, and satisfies  $\mathcal{P}S[U]\mathcal{P}^{-1} = S[U]$ . However, in a numerical simulation those two properties are achieved only in the limit of a large number of gauge field configurations, but are otherwise approximate. Consequently, one should expect that the hybrid meson propagator is contaminated by states of the wrong (positive) parity, albeit with a small amplitude. We will revisit this point in the discussion of results.

With regard to charge conjugation  $\mathcal{C}$  we encounter a similar situation. For the purpose of discussion, changing  $h$  to a charge neutral operator  $h^0$  ( $\bar{d}u \rightarrow \bar{d}d, \bar{u}u$ ), the proof of  $\mathcal{C}O_{h^0}(t)\mathcal{C}^{-1} = -O_{h^0}(t)$  relies on  $\mathcal{C}F_{ij}(x)\mathcal{C}^{-1} = F_{ij}^*(x)$ , which comes from  $\mathcal{C}U_i(x)\mathcal{C}^{-1} = U_i^*(x)$ . Again, at the quantum level the corresponding propagator respects exact (positive) charge conjugation because of  $S[U] = S[U^*]$ . In contrast to the parity case this relation is easily enforced in the simulation. The configurations  $[U]$  and  $[U^*]$  are equally probable. Thus with each  $[U]$  in the ensemble of 200 configurations we also include  $[U^*]$  and compute fermion propagators for both of those. This strategy doubles the number of fermion propagators that need to be computed to 400. However, charge conjugation is now numerically exact, and this also appears to be the reason for an observed noise reduction of simulation signals.

All meson operators  $O_X(t)$ ,  $X = \pi, \rho, a_1, h$ , are expanded by employing quark field smearing [13] and gauge field fuzzing [14].

Smearred quark fields are constructed by spreading the original field  $\psi(x)$  over neighboring sites using a recursive procedure. Define  $\tilde{\psi}^0(x) = \psi(x)$ , then

$$\begin{aligned} \tilde{\psi}^k(x) &= \tilde{\psi}^{k-1}(x) + \sum_{m=1}^3 \alpha_m U_m(x) \tilde{\psi}^{k-1}(x + \hat{m}) \\ &+ \sum_{m=1}^3 \alpha_m U_m^\dagger(x - \hat{m}) \tilde{\psi}^{k-1}(x - \hat{m}), \end{aligned} \quad (4)$$

and similarly for  $\tilde{\bar{\psi}}^k(x)$ , with  $k = 1 \dots K$ . Here  $\alpha_m$  is a strength factor which controls the amount of the smearing in spatial direction  $m$ . To keep the magnitude of the resulting correlation functions numerically under control it is useful to apply a rescaling factor after each smearing step. A suitable choice is motivated by the following observation: For the sake of this argument only, interpret  $\psi, \bar{\psi}$  as Hilbert space operators obeying standard anti-commutation relations, then we find

$$\{\tilde{\psi}^1(x), \tilde{\bar{\psi}}^1(x)\} = \mathbb{1} \left(1 + 2 \sum_{m=1}^3 \alpha_m^2\right), \quad (5)$$

where  $\mathbb{1}$  is the color-spin unit matrix. Thus, with

$$R = \left(1 + 2 \sum_{m=1}^3 \alpha_m^2\right)^{\frac{1}{2}} \quad (6)$$

the smeared quark fields are rescaled as

$$\tilde{\psi}^k \leftarrow R^{-1} \tilde{\psi}^k, \quad \tilde{\bar{\psi}}^k \leftarrow R^{-1} \tilde{\bar{\psi}}^k. \quad (7)$$

after each iteration step (4).

Similarly gauge field fuzzing is implemented defining  $\tilde{U}_m^0(x) = U_m(x)$ , and then adding a sum over staples

$$\begin{aligned} \tilde{U}_m^k(x) &= \tilde{U}_m^{k-1}(x) \\ &+ \sum_{\substack{n=1 \\ n \neq m}}^3 \rho_n [\tilde{U}_n^{k-1}(x) \tilde{U}_m^{k-1}(x + \hat{n}) \tilde{U}_n^{k-1 \dagger}(x + \hat{m}) \\ &+ \tilde{U}_n^{k-1 \dagger}(x - \hat{n}) \tilde{U}_m^{k-1}(x - \hat{n}) \tilde{U}_n^{k-1}(x + \hat{m} - \hat{n})], \end{aligned} \quad (8)$$

with fuzzing strengths  $\rho_m$  in directions  $m = 1, 2, 3$ . Again, for numerical reasons, it is useful to rescale the fuzzy link variables. These are no longer elements of  $SU(3)$ . In particular,

$$\frac{1}{3} \text{Tr} \left( \tilde{U}_m^{k \dagger}(x) \tilde{U}_m^k(x) \right) = S^2, \quad (9)$$

which suggests the normalization prescription

$$\tilde{U}_m^k(x) \leftarrow S^{-1} \tilde{U}_m^k(x) \quad (10)$$

enforcing a trace of one after each fuzzing step (8).

Both normalization prescriptions are clearly invariant under gauge transformations. We use common strength parameters  $\alpha_m = \rho_m = 2.5$  for all spatial directions.

The basis of the current simulation are meson operators  $O_{X\{k\}}(t)$  built from (1) and (2) where  $k = 1 \dots K$  indicates that the quark and gauge fields have been replaced with smeared and fuzzed fields (4) and (8), respectively, at a common level  $k$ . The corresponding, single meson, correlation functions

$$C_{X\{k,l\}}(t, t_0) = \quad (11)$$

$$\langle O_{X\{k\}}(t) O_{X\{l\}}^\dagger(t_0) \rangle - \langle O_{X\{k\}}(t) \rangle \langle O_{X\{l\}}^\dagger(t_0) \rangle$$

are the elements of a  $K \times K$  matrix. We use  $K = 3$ , and unsmeared fields ( $k = 0$ ) are ignored. The same operators are used at both source and sink, so  $C_X(t, t_0)$  is hermitian. Due to our choice of flavor structure (2), the separable terms in (11) are zero.

### III. ANALYSIS

The time evolution of the eigenvalues of  $C_X(t, t_0)$  determines the mass spectrum for the meson  $X$ . Toward extracting the latter a standard procedure would be to solve a generalized eigenvalue problem [15]

$$C_X(t, t_0)\Psi(t) = C_X(t_1, t_0)\Psi(t)\Lambda(t) \quad (12)$$

where  $t_1$  is fixed,  $\Psi(t)$  is a  $K \times K$  matrix, its columns being the generalized eigenvectors, and  $\Lambda(t)$  is real diagonal. This approach is equivalent to a redefinition (linear combination) of the operators that make up the correlator matrix. Its purpose is to improve the numerical ‘quality’ of effective mass function plateaus derived from the eigenvalues.

We shall not rely on effective mass functions here, but rather analyze correlator eigenvalues by means of the maximum entropy method. Within this framework, solving of the generalized eigenvalue problem (12) offers no advantage from a numerical point of view. Thus we will diagonalize  $C_X(t, t_0)$  directly.

Many eigenvalues, behaving exponentially with  $t$ , rapidly vanish into numerical noise. Conventional diagonalization methods do not work well under those circumstances. Singular value decomposition (SVD), on the other hand, is ideally suited to the task [16]. The SVD reads

$$C_X(t, t_0) = U_X(t, t_0) \Sigma_X(t, t_0) V_X^\dagger(t, t_0), \quad (13)$$

where  $U_X(t, t_0)$  and  $V_X(t, t_0)$  are unitary in our case [25], and  $\Sigma_X(t, t_0) = \text{diag}(\sigma_{X;1}(t, t_0) \dots \sigma_{X;K}(t, t_0))$  contains the singular values satisfying  $\sigma_{X;k}(t, t_0) \geq 0$ . The relation of the singular values  $\sigma_{X;k}(t, t_0)$  to the eigenvalues  $\lambda_{X;k}(t, t_0)$  of  $C_X(t, t_0)$  is given by the following theorem: If  $C_X(t, t_0)$  is non-degenerate and positive semi-definite then the set of eigenvalues  $\{\lambda_{X;k}(t, t_0) | k = 1 \dots K\}$  and singular values  $\{\sigma_{X;k}(t, t_0) | k = 1 \dots K\}$  are the same. Proving this is a simple exercise in linear algebra, the columns of  $U_X(t, t_0)$  and  $V_X(t, t_0)$  are eigenvectors which may differ by phase factors only. In case of a degeneracy, which is highly improbable in a numerical setting, the usual ambiguities with respect to eigenvectors apply. For simplicity we will refer to  $\sigma_{X;k}(t, t_0)$  as eigenvalues.

As an example, in Fig. 1 we show all eigenvalues of  $C_X(t, t_0)$  for the hybrid meson operator,  $X = h$ , computed at the smallest pion mass, i.e. the largest  $\kappa$  value. Diagonalization is done independently on each time slice. Note that the eigenvalues are separated by almost three orders of magnitude.

Bayesian analysis methods have been considered for lattice QCD [18, 19, 20, 21, 22, 23], but are not widely used despite obvious advantages. For instance, one may maximize the time slice fitting range. The time slices used for all correlation functions in this work appear in Fig. 1 as filled plot symbols.

The Bayesian fitting problem can be set up and solved in a variety of ways. We here adopt the framework described in detail in Ref. [23]. A brief summary will be

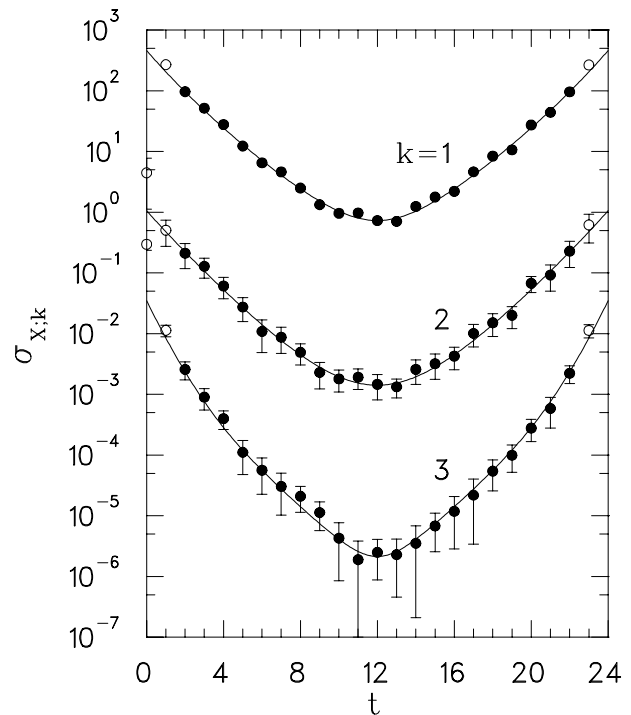


FIG. 1: Eigenvalues of the  $3 \times 3$  correlation matrix  $C_X(t, t_0)$  for the hybrid meson  $X = h$  at the smallest pion mass. Error bars are statistical, derived from a jackknife procedure [17]. The lines are MEM fits as explained in the text. Open plot symbols indicate data points not included in the analysis.

useful: The lattice provides correlation function data, say  $\sigma(t)$ , denoting any set  $\sigma_{X;k}(t, t_0)$  on the given time slice range  $t = 2 \dots 22$ . Our data should be well described by the model

$$F(\rho|t) = \int_0^\infty d\omega \rho(\omega) \cosh(\omega(t - t_c)), \quad (14)$$

where  $t_c = 12$  and  $\rho(\omega)$  is a spectral density function. From the Bayesian perspective the numbers  $\rho(\omega)$  are interpreted as stochastic variables. For these, employing Bayes’ theorem, a conditional probability distribution function  $P[\rho \leftarrow \sigma]$  is constructed. Aside from inessential normalization it has the form

$$P[\rho \leftarrow \sigma] \propto P[\sigma \leftarrow \rho]P[\rho]. \quad (15)$$

Here  $P[\sigma \leftarrow \rho]$  is known as the likelihood function. We construct it from the  $\chi^2$ -distance between the data and the model

$$\chi^2 = \sum_{t_1, t_2} (\sigma(t_1) - F(\rho|t_1)) \Gamma^{-1}(t_1, t_2) (\sigma(t_2) - F(\rho|t_2)), \quad (16)$$

with  $\Gamma(t_1, t_2)$  being elements of the covariance matrix. Then  $P[\sigma \leftarrow \rho] = \exp(-\chi^2/2)$  is the choice for the likelihood function. Bayesian inference uses information one might have about data, for example, a physical upper limit on the spectral masses. Information like this is

contained in  $P[\rho]$ , known as the Bayesian prior. If no prior information is available, except say a physical mass range, a suitable choice is based on the Shannon-Jaynes entropy [11]

$$S = \int_0^\Omega d\omega \left( \rho(\omega) - m(\omega) - \rho(\omega) \ln \frac{\rho(\omega)}{m(\omega)} \right). \quad (17)$$

Here  $\Omega$  is the mentioned cutoff, and the function  $m(\omega)$  is called the default model. It provides a reference point for the spectral density in the sense that  $S \leq 0$ , with  $S = 0$  if  $\rho(\omega) = m(\omega)$ . Then  $P[\rho] = \exp(\alpha S)$  is the choice for the Bayesian prior, introducing a new parameter  $\alpha$ . Hence the conditional probability (15) for the spectral density  $\rho$  becomes

$$P[\rho \leftarrow \sigma] \propto e^{-(\chi^2/2 - \alpha S)}. \quad (18)$$

The idea then is to find a spectral density function  $\rho$  which maximizes  $P[\rho \leftarrow \sigma]$ , the posterior probability, at a fixed data set  $\sigma$ . Bayesian inference within this framework is known as the maximum entropy method (MEM). In [23] it was demonstrated that this problem can be solved by simulated annealing or cooling. Consider the partition function

$$Z_W = \int [d\rho] e^{-\beta_W W[\rho]} \quad \text{with} \quad W[\rho] = \chi^2/2 - \alpha S. \quad (19)$$

It involves the generation of equilibrium configurations  $[\rho]$  while gradually increasing  $\beta_W$  from an initially small value, following some annealing schedule. For details we refer the reader to Ref. [23]. We here only mention that the resulting spectral density  $\rho(\omega)$  is extremely insensitive to both the default model  $m(\omega)$  as well as to the entropy strength parameter  $\alpha$ .

The numerical implementation of the above scheme requires discretization of the  $\omega$  integrals in (14) and (17). Choosing  $a_t \Omega = 2.4$  for the spectral mass cutoff in (17) we use  $a_t \Delta\omega = 0.05$ . The default model is a constant function  $m(\omega) = 10^{-6} a_t$  for all data sets  $\sigma_{X;k}$ , and the entropy strength  $\alpha$  is slightly adjusted, in each case, so as to render the ratio of  $\alpha S$  to  $\chi^2/2$  between 0.1 and 0.01, for the final  $\rho(\omega)$ . Again, those parameter choices may be varied by several orders of magnitude without significantly altering the resulting mass spectrum, see [23] for a discussion.

The spectral density functions  $\rho(\omega)$  for the eigenvalues  $\sigma_{h;k}$ ,  $k = 1, 2, 3$ , of the hybrid meson correlation matrix are displayed in Figs. 2,3,4 respectively. The four panels in each of the figures show the results for the four hopping parameter values as listed in Tab. I below. The top panel, in each case, belongs to the largest  $\kappa$ , or the smallest pion mass, and give rise to the model fits shown as solid lines in Fig. 1. Each spectral density comes from 16 random starts of the annealing process (19). The center histogram (thick solid line) represents the average while the envelope histograms (thin dashed line) indicate the standard deviation with respect to the cooling starts.

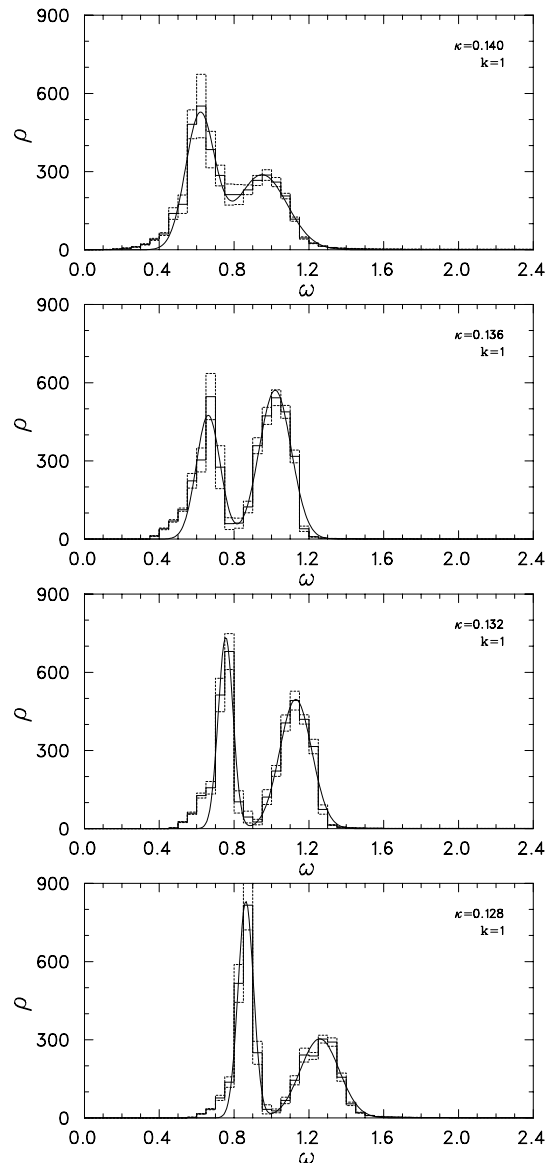


FIG. 2: Spectral density functions (thick solid histogram lines) for the first (largest) eigenvalue set  $\sigma_{h,k}$ ,  $k = 1$ , of the hybrid meson correlation matrix. The four panels correspond to increasing pion masses (decreasing hopping parameters  $\kappa$ ) from top to bottom. The envelope histograms (thin dashed lines) indicate errors as explained in the text. Smooth solid lines correspond to Gaussian fits.

In most cases the spectra exhibit isolated peaks, say  $\delta_n = \{\omega | \omega \in \text{peak } \#n\}$ . Then one may compute, for each peak,  $n = 1, 2$ , the volume  $Z_n$ , the mass  $E_n$ , and the width  $\Delta_n$ , according to

$$Z_n = \int_{\delta_n} d\omega \rho(\omega) \quad (20)$$

$$E_n = Z_n^{-1} \int_{\delta_n} d\omega \rho(\omega) \omega \quad (21)$$

$$\Delta_n^2 = Z_n^{-1} \int_{\delta_n} d\omega \rho(\omega) (\omega - E_n)^2. \quad (22)$$

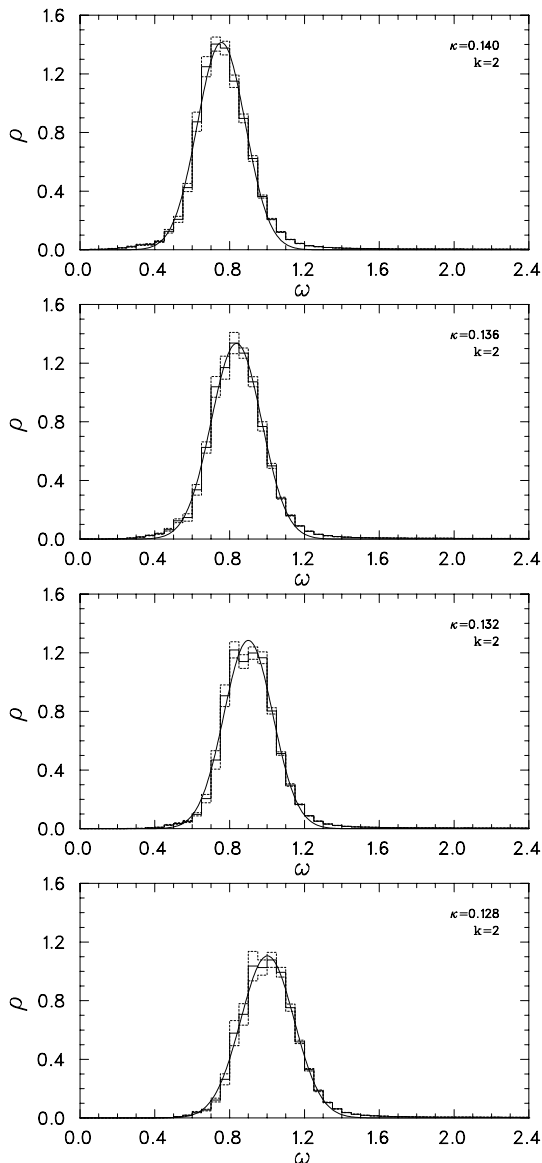


FIG. 3: As Fig. 2, but for the second (intermediate) eigenvalue set  $\sigma_{h,k}$ ,  $k = 2$ .

Those (average) quantities constitute the information that can reasonably be expected to result from the Bayesian analysis.

If overlapping peaks are present the above analysis gives inaccurate results. However, one may then resolve the spectral peaks by fitting a superposition of Gaussians to  $\rho(\omega)$ . Because we are forced to do this in at least one case, see Fig. 2, we have consistently made fits with one or two Gaussians, as required, of all spectral densities for the hybrid meson. To do this a Levenberg-Marquardt algorithm was employed, and the initial set of parameters were conveniently taken from applying (20)–(21). The results of those fits are shown as smooth solid lines in Figs. 2,3,4.

A complete list of the results is given in Tab. I. There,

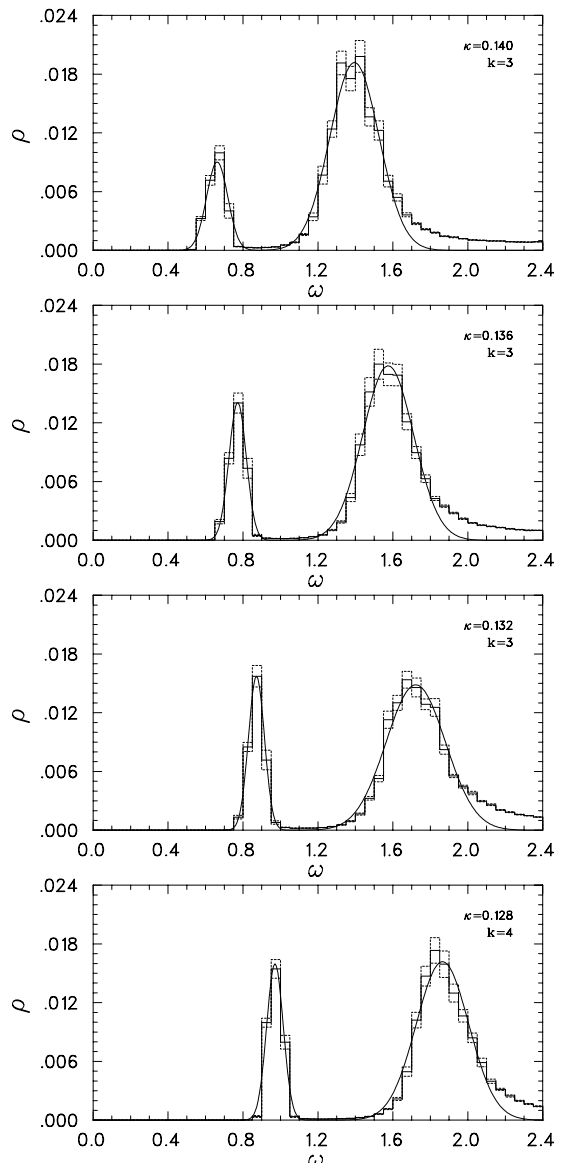


FIG. 4: As Fig. 2, but for the third (smallest) eigenvalue set  $\sigma_{h,k}$ ,  $k = 3$ .

we also show the MEM results for standard mesons  $X = \pi, \rho, a_1$ , which were obtained in the same manner, i.e. from  $3 \times 3$  correlation matrices, etc. The masses of those mesons are used for reference to the physical scale, and extrapolation to the physical pion mass region, as discussed in the next section. The peak volumes  $Z_n$  are related to matrix elements  $\langle n | \Phi_k(t) | 0 \rangle$ , where  $\Phi_k(t)$  is a linear combination of the (three) operators used to construct the correlator matrix [23]. As such they are a measure for how strongly the set of operators excite states  $|n\rangle$  from the vacuum. The overall normalization, however, is arbitrary.

Some comments on uncertainties are in order: As a matter of course jackknife configurations [17] were generated to estimate statistical errors. Those are reflected in

TABLE I: Results of the MEM analysis of correlator matrix eigenvalues for meson operators  $X$  at four values of the hopping parameter  $\kappa$ . The number  $k$  is the eigenvalue label. The entries for the peak volume  $Z_n$ , the peak energy  $E_n$ , and the peak width  $\Delta_n$  for the primary peak  $n = 1$  and secondary peak  $n = 2$ , where appropriate, are the results of Gaussian fits to the computed spectral density functions, see Figs. 2–4. The uncertainties are standard deviations resulting from 16 independent cooling starts. The presence of  $\pm 3$  indicates factors of  $10^{\pm 3}$ .

$X$	$\kappa$	$k$	$n$	$Z_n$	$a_t E_n$	$a_t \Delta_n$
$\pi$	0.140	1	1	18.4(0.8)	0.50(1)	0.0577(1)
	0.136	1	1	17.0(1.4)	0.60(1)	0.0577(6)
	0.132	1	1	16.1(1.4)	0.71(1)	0.057(1)
	0.128	1	1	14.9(1.2)	0.82(1)	0.055(3)
$\rho$	0.140	1	1	46.0(1.9)	0.535(7)	0.072(8)
	0.136	1	1	47.1(0.7)	0.628(8)	0.067(6)
	0.132	1	1	44.4(1.3)	0.725(7)	0.070(8)
	0.128	1	1	42.6(0.5)	0.828(4)	0.067(5)
$a_1$	0.140	1	1	30.1(1.0)	0.69(1) $\circ$	0.13(1)
	0.136	1	1	21.7(0.9)	0.77(1) $\circ$	0.11(1)
	0.132	1	1	17.2(0.4)	0.875(9) $\circ$	0.105(8)
	0.128	1	1	12.8(0.3)	0.979(9) $\circ$	0.096(9)
$h$	0.140	1	1	0.10(6)+3	0.62(4)	0.16(1)
	0.136	1	1	0.08(2)+3	0.66(3)	0.127(9)
	0.132	1	1	0.07(1)+3	0.76(2)	0.079(4)
	0.128	1	1	0.09(1)+3	0.86(2)	0.083(4)
$h$	0.140	1	2	0.10(5)+3	0.95(9)	0.3(2)
	0.136	1	2	0.123(9)+3	1.02(2)	0.17(2)
	0.132	1	2	0.106(8)+3	1.13(2)	0.17(3)
	0.128	1	2	0.079(6)+3	1.26(2)	0.21(3)
$h$	0.140	2	1	0.455(8)	0.756(7)	0.26(2)
	0.136	2	1	0.449(9)	0.837(9)	0.27(2)
	0.132	2	1	0.421(5)	0.900(6)	0.26(1)
	0.128	2	1	0.395(8)	1.002(8)	0.29(2)
$h$	0.140	3	1	1.28(8)–3	0.662(8) $\times$	0.11(3)
	0.136	3	1	1.6(1)–3	0.771(9) $\times$	0.09(3)
	0.132	3	1	1.7(2)–3	0.872(8) $\times$	0.09(3)
	0.128	3	1	1.77(8)–3	0.971(5) $\times$	0.09(2)
$h$	0.140	3	2	6.3(2)–3	1.395(8)	0.26(4)
	0.136	3	2	6.1(2)–3	1.58(1)	0.27(3)
	0.132	3	2	5.9(1)–3	1.72(1)	0.32(2)
	0.128	3	2	5.7(2)–3	1.87(1)	0.28(4)

the error bars of the eigenvalue correlator plots of Fig. 1. However, in the ensuing MEM analysis jackknife errors are hard to maintain, because extraction of the spectral density by way of simulated annealing is very time intensive. (Ideally, the cooling steps should be infinitely small.) For this reason the MEM analysis was only applied to gauge configuration averages. Nevertheless, the peak widths of the spectral density functions naturally emerge as a measure of uncertainties for the masses. One may even argue that those are the ‘true’ measures of uncertainties if compared to statistical (jackknife) errors, because the latter can in principle be made arbitrarily small by increasing the number of gauge configurations, even though the lattice data may be poor. Peak width uncertainties and plateau statistical errors are hard to re-

late, one reason being that they stem from different data sets. This notwithstanding we observe that the masses of Ref. [7], which carry statistical errors, are generally consistent with the ground state meson masses obtained in the current analysis using peak width uncertainties.

#### IV. DISCUSSION OF RESULTS

In order to set the spectral masses into a physical context we have attempted extrapolations to the physical pion mass region. Thus we consider the computed  $\rho, a_1$  and  $h$  spectral masses as functions of  $m_\pi^2$ . To our knowledge, predictions for this dependence from chiral perturbation [24] are not available, as a hybrid meson is involved. We therefore employ a heuristic model. It has been used in Ref. [7], where also some motivation was given. For a spectral mass  $M = a_t m$  we attempt fits with the model

$$M = p + qx + r \ln(1 + x) \quad \text{with } x = (a_t m_\pi)^2, \quad (23)$$

using three parameters  $p, q, r$ . The linear term is standard in  $\chi$ PT inspired models while the logarithmic term is purely heuristical but happens to yield excellent fits to our data. The results are illustrated in Fig. 5.

The extrapolated  $\rho$  meson mass, at  $x = 0$ , is used to determine the physical scale for this simulation. We obtain  $a_t = 0.36(6) \text{ GeV}^{-1} = 0.072(11) \text{ fm}$  ( $m_\rho = 775.8 \text{ MeV}$ ). Table II then gives a list of the extrapolated masses  $a_t E_X$  along with the physical values  $E_X$ . Also listed are estimates of the peak widths at  $x = 0$ . Those are obtained by randomizing the data, replacing the four data points with  $a_t E_n + \xi a_t \Delta_n$  where  $\xi$  is a normal distributed random deviate with variance one, and then repeating the fits with the model (23) obtaining random values for the extrapolated spectral masses  $a_t E_X$ . A few thousand randomizations then give the results  $\Delta_X$  in Tab. II. Uncertainties on  $\Delta_X$ , being second order, were not calculated. The errors given in parentheses are obtained in the same way, but using the uncertainties from Tab. I instead of the  $\Delta_n$ . Unfortunately, extrapolation tends to amplify the peak widths because they become larger at smaller pion masses. As a measure of uncertainty the extrapolated  $\Delta_X$ , in Tab. II, thus seem less useful.

As a first observation we note that the  $a_1$  meson mass in Tab. II comes out very close to the experimental value 1230 MeV, which is the mass of the  $a_1(1260)$  meson, in the nomenclature of [2]. We take this as a hint that the extrapolation model is adequate, and therefore, the extrapolated results for the  $h$  mass spectrum, in Tab. II, may not be without merit.

In the light of this we continue to observe that the energy levels of  $X_{(k,n)}$  for  $h_{(1,1)}$  and  $h_{(2,1)}$  in Tab. II match the experimental masses 1376 MeV and 1653 MeV of the  $1^{-+}$  resonances known as  $\pi_1(1400)$  and  $\pi_1(1600)$  in Ref. [2]. One should not overinterpret the closeness of the computed masses to the experimental levels, because systematic errors associated with the extrapolation could

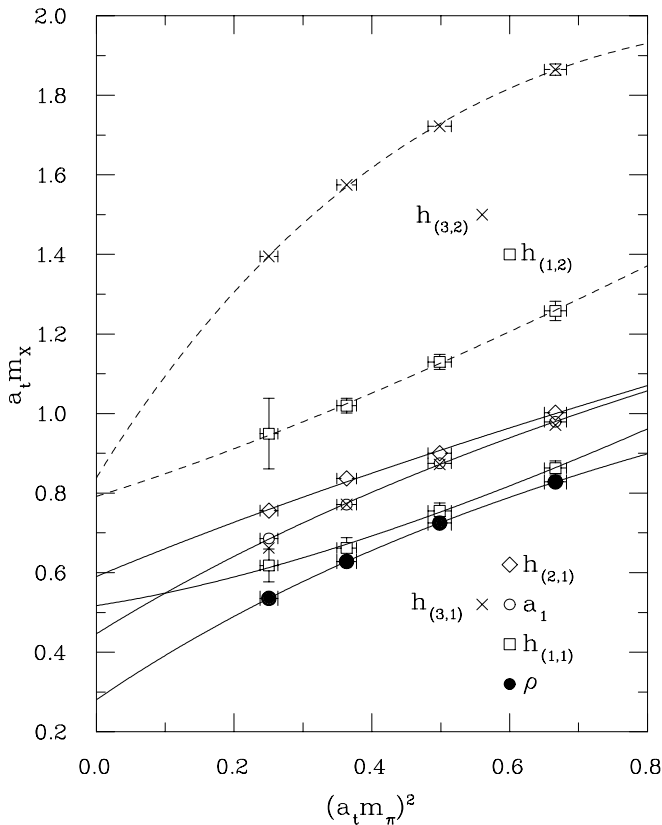


FIG. 5: Plots of spectral meson masses versus the squared pion mass  $x = (a_t m_\pi)^2$  and fits with the model (23). Solid lines refer to masses from primary ( $n = 1$ ) spectral peaks, and dashed lines to secondary ( $n = 2$ ) peaks, see Tab. I. The extrapolation of the  $\rho$  meson mass to  $x = 0$  is used to set the physical scale.

TABLE II: Extrapolated spectral masses  $E_X$  and peak widths  $\Delta_X$ , for mesons  $X$ . The eigenvalue label is  $k$  and the spectral peak number is  $n$ , as in Tab. I. The values for  $\Delta_X$  and for the uncertainties (in parentheses) are obtained by randomization of the data points, as explained in the text.

$X$	$k$	$n$	$a_t E_X$	$a_t \Delta_X$	$E_X$ [GeV]	$\Delta_X$ [GeV]
$\rho$	1	1	0.28(04)	0.08	0.7785	0.22
$a_1$	1	1	0.45(06)	0.17	1.23(0.17)	0.47
$h$	1	1	0.52(19)	0.37	1.43(0.53)	1.03
$h$	1	2	0.79(37)	0.65	2.19(1.03)	1.80
$h$	2	1	0.59(04)	0.27	1.63(0.12)	0.76
$h$	3	1	0.34(05)×	0.20	0.94(0.13)×	0.55
$h$	3	2	0.84(07)	0.11	2.32(0.18)	0.30

be large. On the other hand the spectral level pattern of two  $1^{-+}$  states below 2 GeV is a unequivocal result of this simulation, which in no small part relies on the MEM analysis of the correlator data. It is also interesting to

note that the extrapolated spectral level sequence only emerges beyond the level crossing of the states  $h_{(1,1)}$  and  $a_1$  at around  $x \simeq 0.1$ , see Fig. 5.

Another remarkable result concerns the level  $h_{(3,1)}$ . Its energy spectrum coincides with the one generated by the  $a_1$  meson operator. In Tab. I the symbols  $\circ$  and  $\times$  are attached to the corresponding levels. These are also used in Fig. 5, where an almost perfect match is apparent, only the data point at the smallest pion mass is slightly off. It causes, however, unrealistic extrapolation results, see the entries in Tab. II marked with a  $\times$ . The key to an explanation of this curious result goes back to the observation made in Sect. II, namely that parity is guaranteed only in the limit of a large number of gauge configurations. The level  $h_{(3,1)}$  comes from a correlator eigenvalue about four orders of magnitude less than the dominant one. It may thus single out the contamination of the lattice signal with a  $1^{++}$  state, which happen to be the quantum numbers of the  $a_1$  meson [2]. Although this observation is not directly relevant to our current interest in  $1^{-+}$  exotic states, it nevertheless adds credence to the current simulation and analysis method.

Lastly, the largest levels  $h_{(1,2)}$  and  $h_{(3,2)}$  in Tab. II point at a mass somewhat above 2 GeV. We speculate that at least one of those levels coincides with the  $1^{-+}$  resonance at 1.9 GeV uncovered in Ref. [7]. There the space of operators was larger, including a  $\pi a_1$  two-hadron field in addition to  $h$ , and this could be the cause for a lowering of the energy level from 2 GeV to 1.9 GeV. If this interpretation is correct, then this state likely is a mixture of a hybrid meson and a two-meson state. We take this result as supplementary evidence to the outcome of Ref. [7].

## V. CONCLUSION

Using the maximum entropy method, five distinct spectral levels have been uncovered for the  $J^{PC} = 1^{-+}$  exotic meson. Two of the spectral levels correspond with the  $\pi_1(1400)$  and  $\pi_1(1600)$  from [2]. Two more levels possibly correspond with a resonance energy of 1.9 GeV previously determined by a decay width calculation using Lüscher's method [7]. A fifth spectral level, at higher pion masses, tracks consistent with an operator representing the  $a_1(1260)$  meson, and we take this level to be a consequence of inexact parity symmetry.

All of these spectral levels rely on extrapolations to  $m_\pi = 0$  from relatively heavy pions. Although this may give rise to large systematic errors, the fact that the  $a_1$  extrapolation came very close to its experimental value leads us to conclude at least two spectral levels for the  $1^{-+}$  exotic meson will be below 2 GeV.

[1] T. Barnes (2003), nucl-th/0303032.

[2] S. Eidelman et al., Physics Letters B **592**, 1+ (2004),

URL <http://pdg.lbl.gov>.

- [3] C. Michael, in *23rd International Symposium on Lattice Field Theory, 25-30 July 2005, Trinity College, Dublin, Ireland, PoS(LAT2005)008* (2005), hep-lat/0509023.
- [4] J. N. Hedditch et al., Phys. Rev. **D72**, 114507 (2005), hep-lat/0509106.
- [5] C. W. Bernard et al. (MILC), Phys. Rev. **D56**, 7039 (1997), hep-lat/9707008.
- [6] C. McNeile, Nucl. Phys. **A711**, 303 (2002), hep-lat/0207001.
- [7] M. S. Cook and H. R. Fiebig, Phys. Rev. **D74**, 034509 (2006), hep-lat/0606005.
- [8] C. McNeile and C. Michael (2006), hep-lat/0603007.
- [9] C. McNeile and C. Michael (UKQCD), Phys. Lett. **B556**, 177 (2003), hep-lat/0212020.
- [10] C. McNeile, C. Michael, and P. Pennanen (UKQCD), Phys. Rev. **D65**, 094505 (2002), hep-lat/0201006.
- [11] M. Jarrell and J. E. Gubernatis, Phys. Rep. **269**, 133 (1996).
- [12] R. Gupta, in *Lectures given at the LXVIII Les Houches Summer School: Probing the Standard Model of Particle Interactions* (1998), hep-lat/9807028.
- [13] C. Alexandrou, S. Güsken, F. Jegerlehner, K. Schilling, and R. Sommer, Nucl. Phys. **B414**, 815 (1994), hep-lat/9211042.
- [14] C. Albanese et al., Phys. Lett. **B192**, 163 (1987).
- [15] M. Lüscher and U. Wolff, Nucl. Phys. **B339**, 222 (1990).
- [16] G. H. Golub and C. F. Van Loan, *Matrix Computations* (Johns Hopkins University Press, Baltimore, MD, 1996), 3rd ed., ISBN 0-8018-5413-X.
- [17] B. Efron, SIAM Review 21 (1979) 460.
- [18] T. Yamazaki et al. (CP-PACS), Phys. Rev. **D65**, 014501 (2002), hep-lat/0105030.
- [19] M. Asakawa, T. Hatsuda, and Y. Nakahara, Prog. Part. Nucl. Phys. **46**, 459 (2001), hep-lat/0011040.
- [20] M. Asakawa, Y. Nakahara, and T. Hatsuda, Nucl. Phys. Proc. Suppl. **86**, 191 (2000).
- [21] G. P. Lepage, B. Clark, C. T. H. Davies, K. Hornbostel, P. B. Mackenzie, C. Morningstar, and H. Trottier, Nucl. Phys. Proc. Suppl. **106**, 12 (2002), hep-lat/0110175.
- [22] H. R. Fiebig (LHPC), Nucl. Phys. Proc. Suppl. **106**, 344 (2002), hep-lat/0110163.
- [23] H. R. Fiebig, Phys. Rev. **D65**, 094512 (2002), hep-lat/0204004.
- [24] in *Chiral Dynamics: Theory and Experiment*, edited by A. M. Bernstein and B. R. Holstein (Springer-Verlag, Berlin, Heidelberg, New York, 1995), vol. 452 of *Lecture Notes in Physics*.
- [25] This decomposition easily generalizes to the case of a different number of operators at source and sink.